Key Points:
- Gravity wave potential energy at altitudes from 15 to 70 km is estimated from Rayleigh/Raman lidar observations
- Vertical variation of gravity wave activity in the middle atmosphere over the Antarctic is revealed quantitatively
- Wind filtering of gravity waves with small zonal phase speeds affects the vertical variation of gravity wave activity in early spring

Correspondence to:
M. Kogure,
kogure.masaru@nipr.ac.jp

Rayleigh/Raman lidar observations of gravity wave activity from 15 to 70 km altitude over Syowa (69°S, 40°E), the Antarctic

Masaru Kogure[1,2] [ID], Takuji Nakamura[1,2] [ID], Mitsumu K. Ejiri[1,2] [ID], Takanori Nishiyama[1,2] [ID], Yoshihiro Tomikawa[1,2] [ID], Masaki Tsutsumi[1,2] [ID], Hidehiko Suzuki[3], Takuo T. Tsuda[4] [ID], Takuya D. Kawahara[5], and Makoto Abo[6]

[1]Department of Polar Science, SOKENDAI (The Graduate University for Advanced Studies), Tachikawa, Japan, [2]National Institute of Polar Research, Tachikawa, Japan, [3]Department of Physics, Meiji University Higashi-Mita, Kawasaki, Japan, [4]Department of Computer and Network Engineering, The University of Electro-Communications, Chofu, Japan, [5]Department of Computer Science and Engineering, Shinshu University, Wakasato, Japan, [6]Faculty of System Design, Tokyo Metropolitan University, Hino, Japan

Abstract The potential energy of gravity waves (GWs) per unit mass (E_p), at altitudes of 15–70 km, has been examined from temperature profiles obtained by a Rayleigh/Raman lidar at Syowa Station (69°S, 40°E) from May 2011 to October 2013, with the exception of the summer months. The GWs with ground-based wave periods longer than 2 h and vertical wavelengths between 1.8 and 16 km were extracted from the temperature profiles. E_p was larger in winter than in spring and fall, although in 2012, at altitudes below 30 km, E_p was larger in spring than in winter and fall. E_p increased with a mean scale height of 11.3 km. E_p profiles showed a local maximum at an altitude of 20 km and a minimum at 25 km in almost every month, which has not been reported by previous studies observed by radiosondes. The values of E_p in October of 2012 were smaller at 35–60 km and larger at 20–35 km than those in October of 2011 and 2013. This difference in the E_p profile is most probably caused by different seasonal variations of zonal winds. The larger and smaller E_p values seem to be observed both below and above the altitude at which the zonal wind speed reached 0 m s^{-1}. This result suggests that wind filtering of gravity waves with small phase speeds is significantly important in early spring.

1. Introduction

Gravity waves (GWs) have important roles in transporting energy and momentum vertically between the lower and upaper atmosphere, which influence the atmospheric circulation and temperature structures [*Lindzen*, 1981; *Matsuno*, 1982; *Holton*, 1983; *Fritts and Alexander*, 2003]. Their momentum deposition induces a meridional circulation from the summer pole to the winter pole, which moves the stratospheric temperature distribution in summer and winter away from radiative equilibrium [*Leovy*, 1964; *Holton*, 1983; *Andrews et al.*, 1987]. General circulation models (GCMs) cannot explicitly describe the full spectrum of GWs, owing to the coarseness of their grids, because GWs are a small-scale atmospheric phenomenon. Thus, the GW effect is usually described by parameterizations in GCMs. *Geller et al.* [2013] showed that the GW absolute momentum flux in the stratosphere, simulated by five different GCMs, is at its largest but most uncertain in the winter polar regions, especially in the Southern Hemisphere. They pointed out that the large uncertainty of momentum flux over the high latitude of the Southern Hemisphere in the GCMs is due to the unrealistic representation of GW propagation in their parameterization schemes and a lack of observational constraint on the GW momentum flux over the Antarctic.

GW observations have been performed in the lower, middle, and upper atmospheres of the Antarctic by satellites [*Baumgaertner and McDonald*, 2007; *Alexander et al.*, 2009; *Liu et al.*, 2014], in situ (i.e., radiosondes [*Allen and Vincent*, 1995; *Yoshiki and Sato*, 2000]), and by ground-based instruments (i.e., lidars [*Yamashita et al.*, 2009; *Alexander et al.*, 2011; *Chen et al.*, 2013; *Kaifler et al.*, 2015; *Lu et al.*, 2015; *Chen et al.*, 2016; *Zhao et al.*, 2017] and radars [*Dowdy et al.*, 2007; *Shibuya et al.*, 2015; *Mihalikova et al.*, 2016]). However, most of these observations have a limited range of observable height. Furthermore, it is difficult to quantitatively compare results obtained by different observational techniques, because each observational technique has a different sensitivity to the GW spectrum [*Alexander*, 1998]. Therefore, it is difficult to study vertical

variations of GW activity throughout a wide height range. In particular, the comparison between the lower and upper stratosphere is difficult, because most observational techniques cannot measure the two regions simultaneously. Recently, *Liu et al.* [2014] revealed that the Antarctic and Arctic GW activity of a wide height range varied between 20 and 90 km from Solar Occultation For Ice Experiment (SOFIE)/AIM temperature observations. However, they could not distinguish the latitudinal variations from the seasonal variations because of a limited latitudinal coverage by means of the solar occultation measurements.

A Rayleigh/Raman (RR) lidar installed at Syowa Station can observe the atmospheric temperature over a wide height range (10–80 km altitude) compared to previous observations. This enables us to examine GWs with the same spectral range in vertical wave number from the lower stratosphere (which is closer to source regions of GWs) to the mesosphere, simultaneously.

In this paper, GW activity between the lower stratosphere and the mesosphere over Syowa Station (69°S, 40°E), Antarctic, is investigated using the RR lidar. The vertical and seasonal variations from May 2011 to October 2013 are examined, with the exception of the summer periods, in section 3. In section 4, the GW activity is compared with that of previous studies performed at similar latitudes and is discussed with respect to the zonal winds of Modern-Era Retrospective analysis for Research and Applications (MERRA) [*Rienecker et al.*, 2011], with a particular emphasis on those in October.

2. Observation, Data Sets, and Analysis

A RR lidar, for profiling the atmospheric temperature between 10 and 80 km altitude, was installed in January 2011 at Syowa Station, Antarctic (69°S, 40°E), by the 52nd Japanese Antarctic Research Expedition. The main transmitter is a pulsed neodymium: yttrium/aluminum/garnet laser (355 nm) with a 300 mJ pulse energy and a 20 Hz repetition frequency. The receiver telescope has a primary mirror with an 82 cm diameter and is equipped with three photomultiplier tubes (PMTs). Two PMT channels, the Rayleigh high and low channels, are used to detect the Rayleigh backscattered signal, at 355 nm, from high (23–90 km) and low (10–70 km) altitudes. The other PMT channel, the Raman channel, is used to detect the N_2 vibrational Raman backscattered signal, at 387 nm, between 10 and 40 km altitude. The height and time resolutions of photon counts observed by the RR lidar gave values of 7.5 or 15 m, and 1 min (1200 shots), respectively. Further details and validations of the RR lidar system are described by *Suzuki et al.* [2012]. In this study, the observed photon counts were integrated over a vertical range of 0.9 km and a period of 1 h in order to reduce the uncertainties caused by shot noise. The temperature profiles were then calculated between altitudes of 10 and 80 km from May 2011 to October 2013, excluding the summer periods.

The temperature profiles are calculated from the photon count profiles of the three channels using the Rayleigh integration technique [*Hauchecorne and Chanin*, 1980]. For each photon channel, the photon counts are corrected for extinction, as described in Appendix A. Examples of three temperature profiles obtained using the three channels are shown in Figure 1a. An initial value for Rayleigh integration is given at the highest altitude at which the relative error of the backscattered signal caused by shot noise does not exceed 20% (typically ~90 km altitude for the Rayleigh high channel, ~70 km altitude for the Rayleigh low channel, and ~40 km altitude for the Raman channel). The initial temperature value is taken from CIRA1986 (Committee on Space Research (COSPAR) International Reference Atmosphere) [*Fleming et al.*, 1990] for the Rayleigh high channel. On the other hand, temperatures derived from the Rayleigh high and low channels are used as the initial temperature values for the Rayleigh low and Raman channels, respectively. The temperature profiles obtained from the three observation channels are then merged into one profile, $T(z, t)$, which is used for the investigation of GW activity. The typical temperature errors, using standard deviation, are 6 K at 80 km and no larger than 1 K below 60 km altitude.

Figure 1b shows a merged temperature profile, $T(z, t)$, acquired at 00 UT on 27 June 2012. Figure 1b also shows a temperature profile by a radiosonde observed at the same time as the RR lidar. The two temperature profiles agree well. $T(z, t)$, above a 40 km altitude, is observed by the Rayleigh high channel. Between altitudes of 25 and 40 km, the temperatures derived from the Rayleigh high and low channels are averaged using a weighting of the inverse of the square of the standard deviation of the temperature. Subsequently, for $T(z, t)$ from 25 km to the "merging altitude," the Rayleigh low channel is used. Between the merging altitude and 10 km, the Raman channel is used. At the merging altitude and two adjacent heights (above and below),
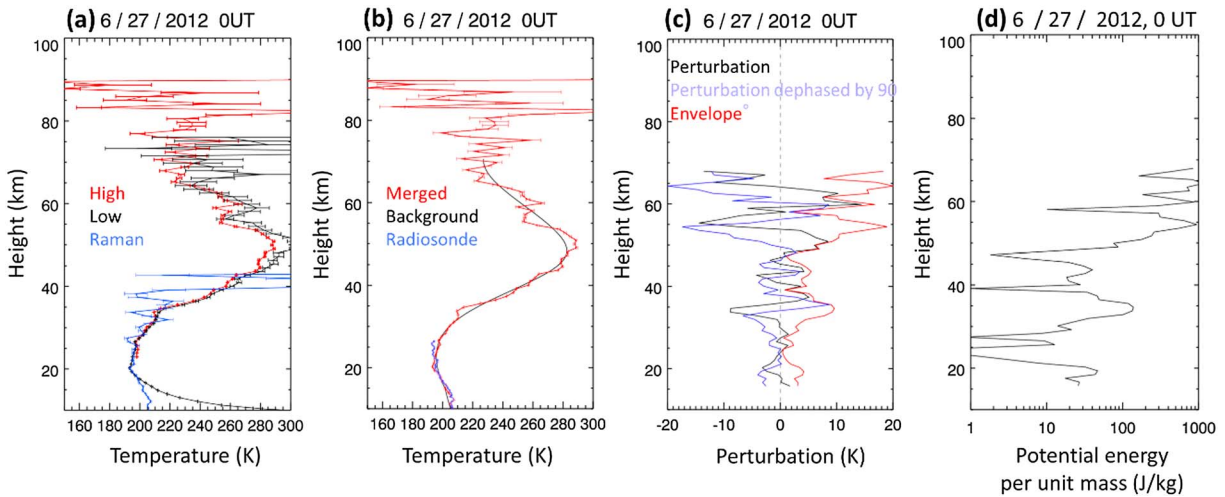
Figure 1. (a) Temperature profiles observed using the Rayleigh high (red), Rayleigh low (black), and Raman channels (blue) at 23:30–24:30 UT on 27 June 2012 at Syowa Station. The horizontal bars indicate standard deviation errors caused by shot noise. (b) Merged temperature (red) and estimated background temperature (black) profiles obtained by the lidar. The blue line indicates a temperature profile obtained by the concurrent radiosonde observation. (c) Temperature perturbation (black), its Hilbert transform (blue), and envelope (red). (d) Instantaneous E_p profile (see the text for details).

$T(z, t)$ is given as an averaged temperature between the Rayleigh low and Raman channels. The merging altitude is selected to be between 10 and 20 km, so that the mean square of the temperature difference between the Rayleigh low and Raman channels in the 2.7 km height range is minimized. In Figure 1b, the merging altitude was selected to be 19.35 km. Note that in the presence of polar stratospheric clouds (PSCs) with a backscatter ratio (BSR) larger than 1.05, the merging altitude is selected to be above the top of the PSCs. The BSR was calculated from the ratio of the signal intensities of the Rayleigh low and Raman channels [*Ansmann et al.*, 1992].

The temperature perturbation $T'(z, t)$ is calculated as

$$T'(z, t) = T(z, t) - T_0(z, t), \tag{1}$$

where $T_0(z, t)$ is the background temperature profile. $T_0(z, t)$ is derived from each temperature profile, $T(z, t)$, at a time, t, based on a method introduced by *Duck et al.* [2001] and *Ehard et al.* [2015]. In a window with a 24 km altitude range, the temperature profile is fitted by a cubic polynomial function. Subsequently, the window is shifted by a 0.9 km step to obtain the fitted profiles. The fitted temperature values at each height are averaged with an emphasis on the central 8 km in the profile fittings. Details of the weighting function are found in *Duck et al.* [2001]. Finally, the weighted average profile is smoothed by applying a 5.4 km running average. Further details of this method are described by *Duck et al.* [2001]. Note that the above process extracts the temperature perturbations of GWs with vertical wavelengths (λ_z) of 1.8–16 km. It is also noteworthy that GWs with periods (τ) longer than 2 h (the Nyquist period) were extracted as well. Examples of two temperature profiles, $T(z, t)$ and $T_0(z, t)$, acquired at 00 UT on 27 June 2012, are shown in Figure 1b, and the resultant $T'(z, t)$ profiles are plotted in Figure 1c.

The potential energy of GWs per unit mass, $E_p(z)$, is calculated as described in *Whiteway and Carswell* [1994]:

$$E_p(z) = \frac{1}{2}\left(\frac{g}{N(z)}\right)^2 \overline{\left(\frac{T'^2(z,t)}{T_0^2(z,t)}\right)}, \tag{2}$$

where g is the gravitational acceleration (9.8 m s^{-2}). $N(z)$ is the Brunt-Väisälä frequency, derived as

$$N^2(z) = \frac{g}{\overline{T_0(z,t)}}\left[\frac{\overline{dT_0(z,t)}}{dz} + \frac{g}{C_p}\right], \tag{3}$$

where C_p is the dry air specific heat at constant pressure (1005 J kg^{-1}K^{-1}). The $\frac{\overline{dT_0(z,t)}}{dz}$ is calculated using a linear least squares fit over a 10 km height range. The overbars in equations (2) and (3) indicate the nightly

Table 1. Table of RR Lidar Observations From May 2011 to October 2013 Used in This Study

	Year	Feb	Mar	Apr	May	Jun	Jul	Aug	Sep	Oct	Total
Observations	2011	0	0	0	6	1	8	11	10	8	44
Observation hours		0	0	0	53	9	108	85	79	42	376
Observations	2012	3	3	9	10	12	7	6	17	10	77
Observation hours		15	20	72	116	153	95	77	181	47	776
Observations	2013	0	7	12	9	10	13	4	10	6	71
Observation hours		0	40	109	120	138	173	47	96	33	756
Observations	Total	3	10	21	25	23	28	21	37	24	192
Observation hours	Total	15	60	181	289	300	376	209	356	122	1908

mean. The Fourier components of $T'(z,t)$ and its Hilbert transform, $T'_h(z,t)$, have the same amplitude and are out of phase by $90°$ [*Bracewell*, 1999]:

$$\overline{T'^2(z,t)} = \overline{T'^2_h(z,t)}. \tag{4}$$

Thus, $E_p(z)$ is also written as

$$E_p(z) = \frac{1}{2}\left(\frac{g}{N(z)}\right)^2\left[\frac{1}{2}\left(\frac{\overline{T'^2(z,t) + T'^2_h(z,t)}}{T_0^2(z,t)}\right)\right]. \tag{5}$$

$T'_h(z,t)$ is calculated as

$$T'_h(t,z) = \frac{\mathscr{H}\left(T'(z,t)F(z)\right)}{F(z)}, \tag{6}$$

where $\mathscr{H}$ indicates a Hilbert transform operator. $F(z)$ is a weighting function to suppress the exponential growth of the temperature perturbation, $T'(z,t)$, with altitude and is given by $F(z) = \rho_{(z)}^{1/4}$, where $\rho(z)$ is the atmospheric density obtained from the CIRA1986 reference model [*Fleming et al.*, 1990]. Figure 1c shows $T'_h(z,t)$ and an envelope ($\sqrt{T'^2(z,t) + T'^2_h(z,t)}$). If the observation time is long, such that the number of samples for the ensemble average is sufficiently large, equations (2) and (5) yield the same results. However, the statistical error for E_p in equation (5) is smaller than that in equation (2), because the number of samples for the ensemble average in equation (5) is twice as large as that in equation (2).

Figure 1d shows an instantaneous E_p profile obtained by the RR lidar at 00 UT on 27 June 2012. Apart from the perturbation due to GWs, $T'(z,t)$ also includes the error caused by photon counting noise (or shot noise). Therefore, a positive bias of E_p could be caused [*Duck et al.*, 2001; *Chu et al.*, 2009; *Yamashita et al.*, 2009]. However, this additional variance of $T'(z,t)$ could be estimated independently. Thus, the corrected E_p values are now estimated in equation (5).

Table 1 shows the total observation time and the number of nights in each month used for this analysis. The observational data with durations longer than 3 h are used for analysis when the hourly temperature error is smaller than 6 K at a 65 km altitude. Height regions with temperature errors larger than 1 K are excluded from the $E_p(z)$ analysis in order to avoid overestimation of $E_p(z)$ at these altitudes for the temperatures derived from Raman channel.

3. Results

3.1. Monthly Mean Temperature

Figure 2 shows the monthly mean temperature observed by the RR lidar over Syowa from 2011 to 2013. The mean temperature showed similar seasonal and vertical variations each year. The stratopause, where the temperature reached its maximum value, was the highest (~55 km in altitude) and the coldest (250–260 K) around April in 2 years (2012 and 2013). The stratopause height descended from April to October with increasing temperature. A cold region with a temperature of approximately 190 K or less was observed at around 20 km from June through to August, which suggests the possibility of PSC formation above Syowa. The observed temperature structures are similar to those over the southern polar region [*Hitchman et al.*, 1989; *France et al.*, 2012] and Davis station (69°S, 78°E) [*Alexander et al.*, 2011].
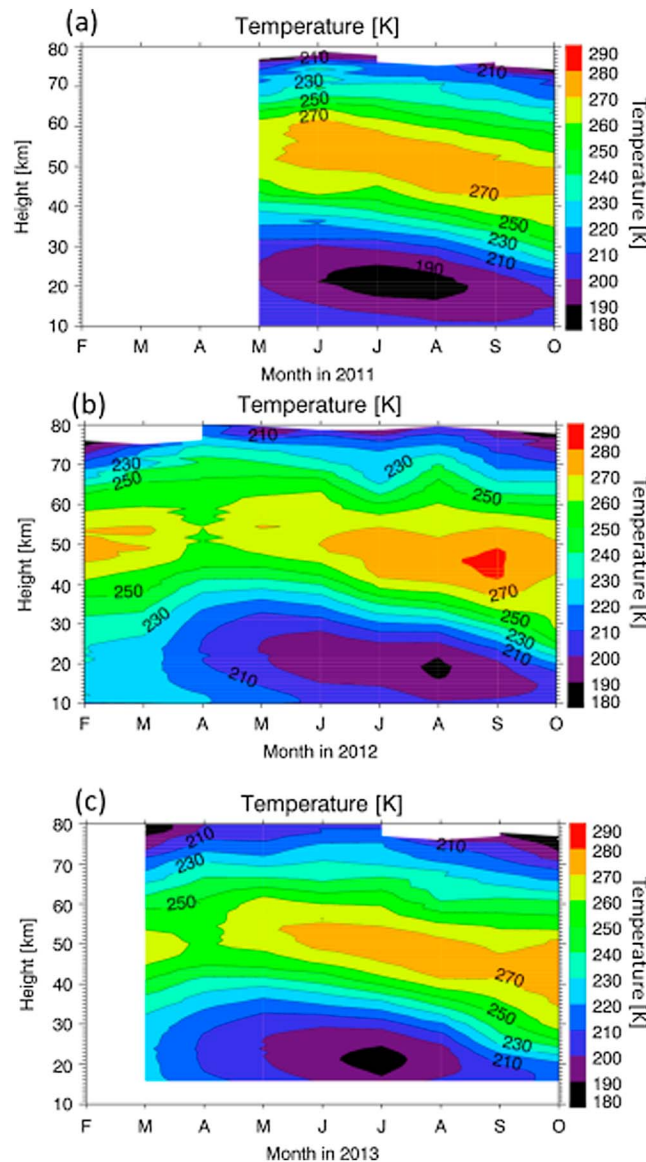
Figure 2. Time-altitude sections of monthly mean temperature acquired using the RR lidar observations in (a) 2011, (b) 2012, and (c) 2013.
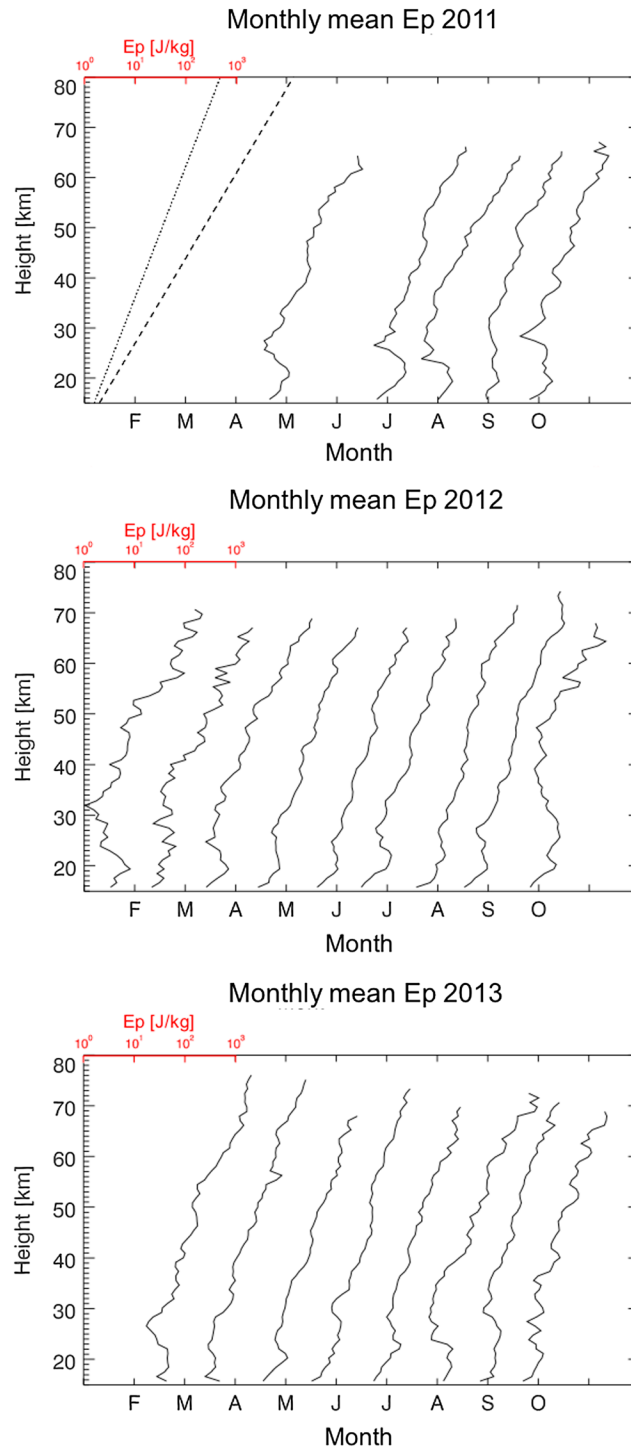
3.2. Monthly Mean E_p

Profiles of monthly E_p values between 2011 and 2013 are shown in Figure 3. The E_p profile in June of 2011 was excluded, because the statistical fluctuation was too large owing to the limited observation time (see Table 1).

Almost all E_p profiles in Figure 3 had a roughly constant exponential slope above an altitude of 30 km. The mean scale height between 35 and 64 km was 11.3 km as an average over 3 years, with a standard deviation of 2.6 km. The dotted line in Figure 3 indicates the 11.3 km scale height. The dashed line in Figure 3 indicates the slope of the density scale height, $H = 7.3$ km, which was calculated from the mean temperature between 30 and 70 km over 3 years. This value is smaller than the scale height of E_p.

Another distinct feature of the E_p profiles in Figure 3 is that most of them had local maxima at altitudes of approximately 20 km and local minima at altitudes around 25 km. On the other hand, the E_p profile in October of 2012 (the right-most panel in Figure 3b) had a local minimum around 40 km, which is much higher than those of the other months.

Figure 4 shows time-altitude sections of the monthly mean E_p from 2011 to 2013. Figure 5 shows day-to-day variations of E_p at 20, 40, and 60 km altitudes. The E_p values were logarith-mically averaged over a height range of 5.4 km centered at the target height. E_p above 30 km altitude was maximized in winter (June, July, and August). E_p below 30 km altitude was also maximized in winter (July and August). However, in 2012, the E_p below 30 km had another maximum in October. The interannual variations were smaller than the seasonal variations, and the day-to-day variations are within a factor of 3 to 4.

4. Discussion

4.1. Comparison of E_p Above 30 km Over the Antarctic

Here we compare our results with other lidar and satellite observations over other locations in the Antarctic. These include Rayleigh lidar observations over Davis (69°S, 78°E) [*Alexander et al.*, 2011; *Kaifler et al.*, 2015], Rothera (67°S, 68°W) [*Yamashita et al.*, 2009] and McMurdo (78°S, 167°E) [*Lu et al.*, 2015], and SOFIE/AIM observations between ~63 and 78°S latitude [*Liu et al.*, 2014]. It should be noted that vertical wavelengths and ground-based periods of the extracted GWs were slightly different among these studies. Our study extracted the GWs with λ_z of 1.8–16 km and τ longer than 2 h. *Alexander et al.* [2011] and *Kaifler et al.* [2015] extracted

Monthly mean Ep 2011

Monthly mean Ep 2012
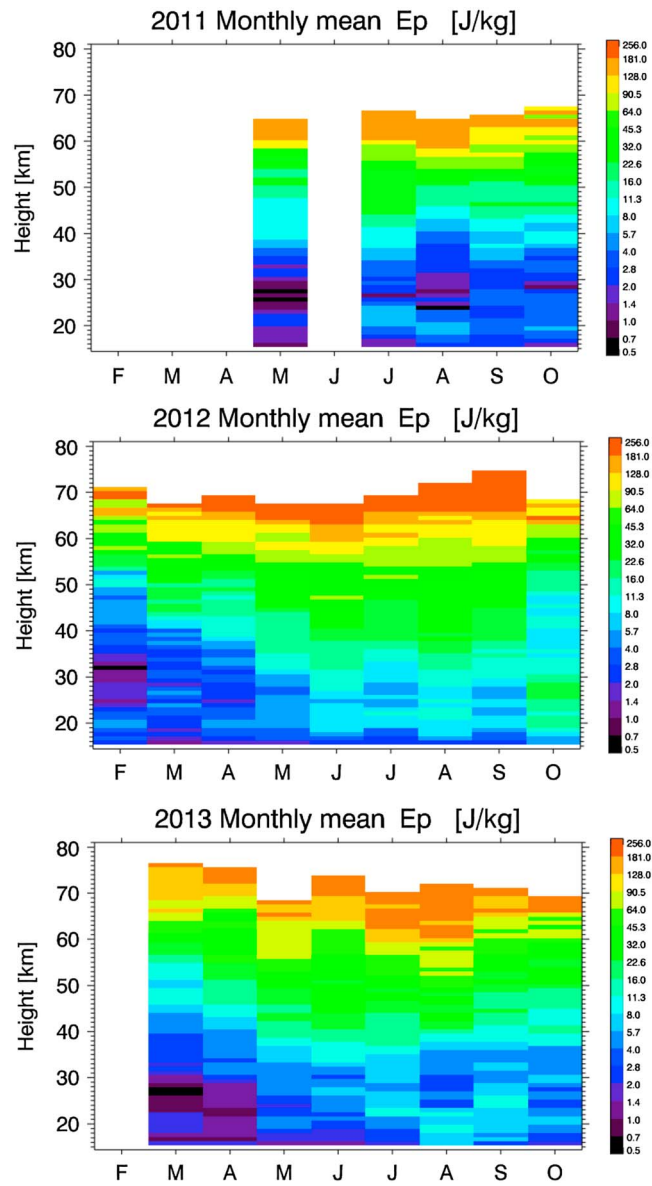

Monthly mean Ep 2013

Figure 3. Time series of monthly mean E_p profiles in (a) 2011, (b) 2012, and (c) 2013. The profiles are shifted by 10^1 intervals for each month. The dashed and dotted lines indicate the slope of the density scale height (H = 7.3 km, H is calculated from mean temperature between 30 and 70 km over 3 years) and the slope of the mean E_p scale height, respectively.

the GWs with λ_z of 4–20 km and τ longer than 2 h. *Yamashita et al.* [2009] extracted those with λ_z of 2–15 km and τ of 1–3 h, and *Lu et al.* [2015] extracted those with λ_z of 2–15 km (i.e., same as *Yamashita et al.* [2009]) and τ of 2–15 h. Although *Liu et al.* [2014] extracted those with λ_z of 2–15 km (i.e., similar to the lidar observations), their horizontal wavelengths are longer than 580 km. This is because the horizontal path length of SOFIE/AIM is approximately 290 km [*Stevens et al.*, 2012]. The seasonal variation of E_p above 30 km over Syowa showed a maximum value in winter. The maximum is consistent with those acquired at Davis and Rothera, as well as the result of the SOFIE/AIM observations.

The E_p profiles over Syowa in 2011 (purple), 2012 (green), and 2013 (yellow) between May and August are shown in Figure 6. The E_p profile over Davis in 2011 is represented by the blue line [*Kaifler et al.*, 2015]. The average profile over Davis in 2007 and 2008 is also indicated in black, as a reference [*Alexander et al.*, 2011]. The scale height of E_p over Syowa between 35 and 64 km in 2011 and 2012 are 9.7 km and 13.7 km, respectively. The scale height in 2013 (13.3 km) is similar to that in 2012. The two profiles acquired over Davis are almost identical, and therefore, the result in 2011 is a typical profile. The scale height of E_p was ~6.8 km between altitudes of 30 and 40 km and close to the density scale height. Thus, the scale height of E_p is larger over Syowa than over Davis. The E_p profile taken by SOFIE/AIM (red) for 2007–2013 shows a scale height of 13 km [*Liu et al.*, 2014]. The scale height over McMurdo in 2011 and the average of 2011–2013 are 12.2 and 13 km, respectively (plots not shown here) [*Lu et al.*, 2015]. Subsequently, we can say that the scale height of E_p over Syowa is close to those acquired over McMurdo and by SOFIE/AIM observations and that the scale height taken over Davis is much smaller. This is an interesting result because Syowa and Davis are at almost the same latitude and only 1500 km apart.

Figure 4. Time-altitude sections of monthly mean E_p in (a) 2011, (b) 2012, and (c) 2013. The E_p in June of 2011 has been removed, owing to insufficient observation time.
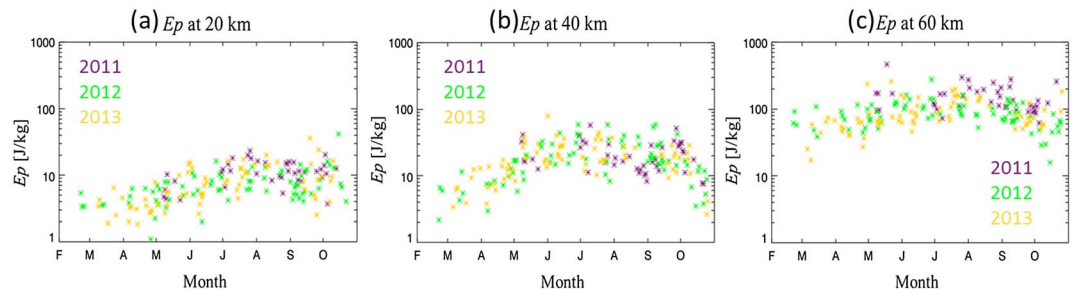
Figure 5. Seasonal variations of nightly mean E_p at (a) 20 km, (b) 40 km, and (c) 60 km. The blue, yellow, and green asterisks indicate the E_p values in 2011, 2012, and 2013, respectively.
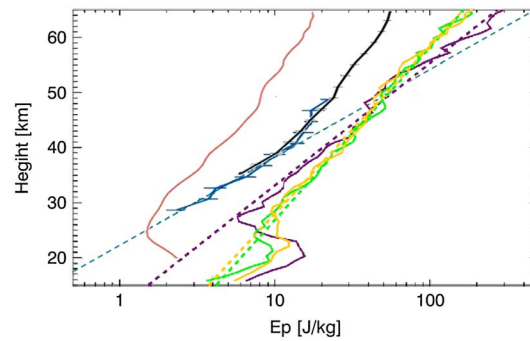
Figure 6. Comparison of E_p profiles. The red line is a mean E_p profile in winter over 63–78°S during 2007–2013 estimated from temperatures observed by SOFIE/AIM [*Liu et al.*, 2014]. The black and blue lines are mean E_p profiles over Davis during 2007–2008 and 2011, respectively [*Alexander et al.*, 2011; *Kaifler et al.*, 2015]. The blue dashed line indicates a slope of the E_p between 29 and 40 km altitude [*Kaifler et al.*, 2015]. The green, purple, and yellow lines are mean E_p profiles in winter over Syowa during 2011, 2012, and 2013, respectively. The green, purple, and yellow dashed lines indicate their corresponding linear fittings.

It should be noted that the observed absolute E_p values are somewhat different among our study and previous studies (e.g., the value of E_p at 40 km in 2011 was 22 J kg^{-1} over Syowa but was 12 J kg^{-1} over Davis [*Kaifler et al.*, 2015]). This is probably due to the different vertical resolutions and preprocessing. The height resolution used in *Kaifler et al.* [2015] was 2 km, which was coarser than ours (0.9 km). If a vertical resolution of 2 km is applied, the E_p value over Syowa would be 18 J kg^{-1}. In addition, *Kaifler et al.* [2015] applied a high-pass filter with a cutoff wavelength of 20 km to the temperature perturbation profiles, which was not used in our analysis. The E_p value over Davis would be 15 J kg^{-1} without the high-pass filter. The actual difference would be 20% and should not be significant.

4.2. Seasonal and Vertical Variations of E_p Below 30 km

In section 3.2, our results over Syowa indicated a peak and a local minimum of E_p at approximate altitudes of 20 and 25 km, respectively. However, the previously reported E_p profile over Syowa, acquired using radiosondes, did not show a similar local peak below 25 km [*Yoshiki and Sato*, 2000; *Yoshiki et al.*, 2004]. The height range of our observation was 10–80 km, while the radiosonde observed between 0 and 30 km. It should also be noted that our analysis used an hourly averaged temperature, while the radiosonde samples used instantaneous temperature without time averaging. The height average for our lidar was over 0.9 km. Such a difference could cause different spectral bands to be extracted (in both the time and altitude domains), together with the different analysis procedures [*Wright et al.*, 2015].
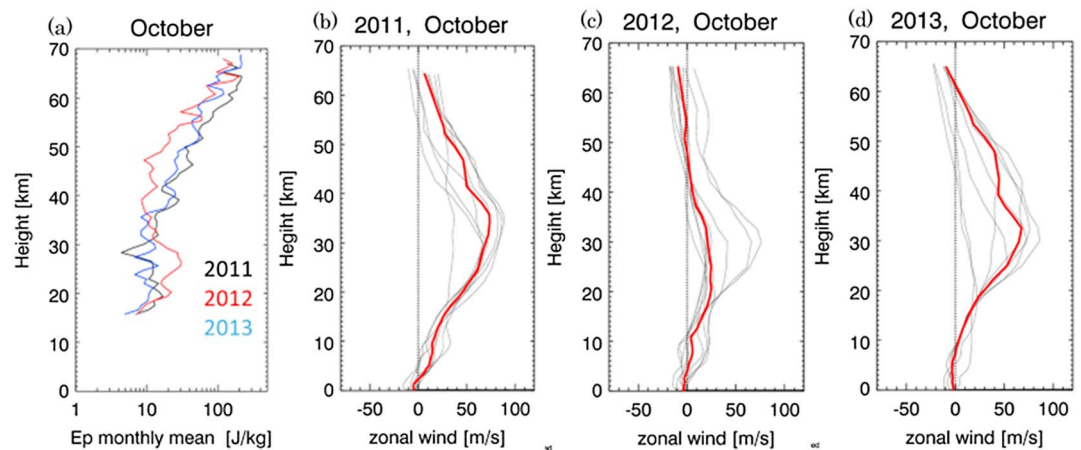
Figure 7. (a) Monthly mean E_p in October of 2011 (black), 2012 (red), and 2013 (blue). (b–d) Nightly mean zonal winds from MERRA over Syowa Station on the observation dates in 2011 (Figure 7b), 2012 (Figure 7c), and 2013 (Figure 7d). The red lines represent a median profile of October for each year.
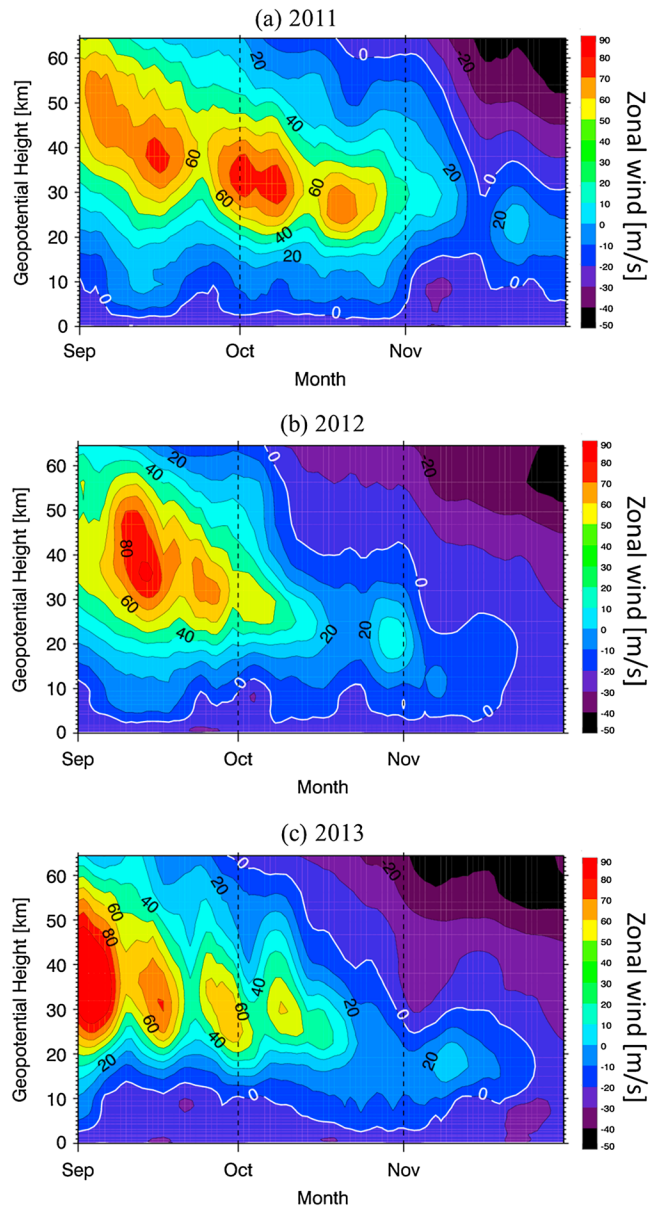
Figure 8. Time-height sections of weekly running averaged zonal wind obtained from MERRA over Syowa from September to November in (a) 2011, (b) 2012, and (c) 2013. The *x* axis indicates the mean geopotential height in September to November. The dashed lines represent the first day of each month. The thick white lines indicate 0 m s^{-1}.

Our results showed that GWs with a longer period (>2 h) and a large vertical wavelength (>1.8 km) showed a clear peak in E_p around a 20 km altitude. *Shibuya et al.* [2015] reported that an inertia-GW was generated through the spontaneous adjustment in the area west of Syowa and propagated through the lower stratosphere over Syowa. Such GWs possibly contribute to the local maximum.

4.3. Characteristic E_p Profile in October of 2012

As mentioned in the previous section, the monthly mean E_p profile in October of 2012, obtained by the RR lidar, was different from those of the other months. Figure 7a shows monthly mean E_p profiles acquired using our RR lidar in October from 2011 to 2013. The E_p profile in 2012 is smaller than those in 2011 and 2013 above 35 km altitude. On the other hand, the E_p profile in 2012 has a clear maximum around 25 km, unlike in 2011 and 2013. Such characteristics of E_p in 2012 were not due to an outstanding GW event on a single day but were seen for 6–16 October 2012 (i.e., four observation days). In order to examine the relationship between the E_p profiles and zonal wind distributions, nightly mean zonal wind profiles on the nights of lidar observations, together with the monthly medians in October from 2011 to 2013, were obtained from MERRA [*Rienecker et al.*, 2011] and are shown in Figures 7b–7d. The zonal wind at altitudes of 40–50 km altitude in October was close to 0 m s^{-1} on many nights in 2012. However, it was larger than 30 m s^{-1} on most nights in 2011 and 2013. The comparison between E_p and the zonal wind suggests that GWs with a small ground-based eastward phase speed (i.e., < ~20 m s^{-1}) reached their critical level at altitudes of approximately 40–50 km and were prohibited from propagating upward in October of 2012. Such a wave could converge below the critical level and obtain a large amplitude or a large E_p value.

Figure 8 shows zonal wind speeds, with a smoothing window of 7 days, over Syowa from September to November in 2011–2013. In 2012, the altitude at which the zonal wind speed was 0 m s^{-1} moved down to 40 km on 10 October. Such descents were observed in mid-November of 2011 and in late October of 2013. Thus, the time of descent of the 0 m s^{-1} wind line controls the vertical and seasonal variations in E_p in early spring. These results also suggest that the GWs with a small ground-based zonal phase speed occupy a

large part of the E_p obtained by the RR lidar. We would like to note that *Kaifler et al.* [2015] also observed a decrease of E_p above the altitude of the weak zonal wind over Davis, Antarctica, in November of 2011.

5. Conclusion

In this study, GWs with a period longer than 2 h and a vertical wavelength of 1.8–16 km were extracted from temperature profiles obtained by the RR lidar over Syowa Station (69°S, 40°E) between May 2011 and October 2013 in the nonsummer months. E_p was estimated for a wide range of altitudes, 15–70 km, to reveal seasonal and vertical variations in GW activity.

Four features of E_p were revealed: (1) The GW activity was greater in winter than in spring and fall, although in 2012, below an altitude of 30 km, the activity was greater in spring than in winter and fall. The seasonal variation above 30 km is in good agreement with previous studies using a Rayleigh lidar at other Antarctic stations. (2) The E_p values above 30 km in altitude increased with a mean scale height of 11.3 km. This scale height over Syowa during winter compared well with observations over Davis, McMurdo, and SOFIE/AIM observations over ~63 and 78°S latitude. However, the scale height over Davis (~6.8 km) was smaller and close to the density scale height, although Syowa and Davis are located relatively close to each other (~1500 km apart). (3) The E_p profiles had local maxima at altitudes around 20 km and local minima at altitudes around 25 km in almost all months. This feature was persistent but not yet reported by the previous radiosonde studies [*Yoshiki and Sato*, 2000]. Although it is not clear how the local maxima of E_p around 20 km are created, GW packets generated by spontaneous adjustment in the east of Syowa [*Shibuya et al.*, 2015] could contribute to the local maxima. (4) The E_p in October 2012 was smaller at altitudes of 35–60 km and larger at altitudes of 20–35 km, compared with 2011 and 2013. We found that the critical level at which the zonal wind weakens in October 2012, which is different from the other years, caused this particular structure.

The RR lidar enabled us to analyze GWs in a wide height range using the same observation and analysis method. This study revealed many features of E_p from the lower stratosphere to the mesosphere over Syowa station that will contribute to understanding of GW vertical propagation, the coupling between lower and upper atmospheres, and the relationship between GWs and background winds in early spring. Moreover, we revealed that the scale heights between Syowa and Davis are quite different, although the two stations are located relatively close to each other. The reason for this difference will be studied using more observation data acquired using different measurement techniques in the future.

Appendix A

Atmospheric extinction over Syowa is calculated for altitudes between 10 and 90 km in order to correct the photon counts attenuated by extinction. The extinction profile in an altitude range of 20–90 km is calculated based on the method introduced by *Hauchecorne and Chanin* [1980]. Namely, the extinction profiles are estimated using atmospheric Rayleigh scattered extinction, because Mie scattered extinction is significantly small. The atmospheric density is obtained from radiosonde observation in an observable range and CIRA1986 (COSPAR International Reference Atmosphere) [*Fleming et al.*, 1990] from the top of the radiosonde observable range to an altitude of 90 km. A Rayleigh scattered extinction coefficient is calculated as in *Bucholtz* [1995]. The extinction profiles between altitudes of 10 and 20 km, for the photon count profiles of the Rayleigh low channel, are calculated using the same method as used in the upper region. On the other hand, the extinction profile for the photon count profile of the Raman channel between altitudes of 10 and 20 km is determined by the total extinction coefficient, which includes Mie scattered extinction, because Mie scattered extinction in the lower stratosphere cannot typically be neglected.

The total extinction for the photon count profile of the Raman channel between altitudes of 10 and 20 km is calculated based on the method introduced by *Ansmann et al.* [1990] in order to examine the total extinction profile in that region. The total round-trip extinction coefficient, $\alpha_{\text{total}}(z)$, is written as

$$\alpha_{\text{total}}(z) = \alpha_{355}(z) + \alpha_{387}(z) = \frac{d}{dz}\ln\left(\frac{O(z)n(z)}{z^2 P(z)}\right),$$

where $\alpha_{355}(z)$ and $\alpha_{387}(z)$ are the total extinctions at wavelengths of 355 nm and 387 nm, respectively. $O(z)$ is

an instrumental field-of-view function, typically with a value between altitudes of 10 and 20 km. The $n(z)$ is the atmospheric density obtained from a radiosonde observation acquired at 0 UT, and $P(z)$ is the Raman signal at a 387 nm wavelength between 23:30 and 00:30 UT. The $\alpha_{total}(z)$ is calculated using a linear least squares method, assuming that the ratio of the Mie extinction to the atmospheric extinction is constant between altitudes of 10 and 20 km. The total extinction profile between altitudes of 10 and 20 km can be determined from $\alpha_{total}(z)$ and the atmospheric density obtained by the radiosonde observation.

The difference between the temperature obtained by the radiosonde observation and the Raman channel using the total extinction profile is smaller than 1 K between altitudes of 10 and 20 km, though the temperature obtained by the Raman channel, neglecting Mie extinction, is ~3 K colder around 15 km and ~6 K colder around 10 km than radiosonde observations, on average. The $\alpha_{total}(z)$ can be applied to all Raman signal profiles during the night, assuming that the time variation of the total extinction between altitudes of 10 and 20 km is significantly smaller during the night.

References

Alexander, M. J. (1998), Interpretations of observed climatological patterns in stratospheric gravity wave variance, *J. Geophys. Res.*, *103*(D8), 8627–8640, doi:10.1029/97JD03325.

Alexander, S. P., A. R. Klekociuk, and T. Tsuda (2009), Gravity wave and orographic wave activity observed around the Antarctic and Arctic stratospheric vortices by the COSMIC GPS-RO satellite constellation, *J. Geophys. Res.*, *114*, D17103, doi:10.1029/2009JD011851.

Alexander, S. P., A. R. Klekociuk, and D. J. Murphy (2011), Rayleigh lidar observations of gravity wave activity in the winter upper stratosphere and lower mesosphere above Davis, Antarctica (69°S, 78°E), *J. Geophys. Res.*, *116*, D13109, doi:10.1029/2010JD015164.

Allen, S. J., and R. A. Vincent (1995), Gravity wave activity in the lower atmosphere: Seasonal and latitudinal variations, *J. Geophys. Res.*, *100*(D1), 1327–1350, doi:10.1029/94JD02688.

Andrews, D., J. Holton, and C. Leovy (1987), *Middle Atmosphere Dynamics*, Academic Press, Orlando, Fla.

Ansmann, A., M. Riebesell, and C. Weitkamp (1990), Measurement of atmospheric aerosol extinction profiles with a Raman lidar, *Opt. Lett.*, *15*, 746–748.

Ansmann, A., M. Riebesell, U. Wandinger, C. Weitkamp, E. Voss, W. Lahmann, and W. Michaelis (1992), Combined Raman elastic-backscatter lidar for vertical profiling of moisture, aerosol extinction, backscatter, and lidar ratio, *Appl. Phys. B: Lasers Opt.*, *55*(1), 18–28.

Baumgaertner, A. J. G., and A. J. McDonald (2007), A gravity wave climatology for Antarctic compiled from Challenging Minisatellite Payload Global Positioning System (CHAMP/GPS) radio occultations, *J. Geophys. Res.*, *112*, D05103, doi:10.1029/2006JD007504.

Bracewell, R. (1999), The Fourier transform and its applications, p. 640, McGraw-Hill Education.

Bucholtz, A. (1995), Rayleigh-scattering calculations for the terrestrial atmosphere, *Appl. Opt.*, *24*, 2765–2773.

Chen, C., X. Chu, A. J. McDonald, S. L. Vadas, Z. Yu, W. Fong, and X. Lu (2013), Inertia-gravity waves in Antarctica: A case study using simultaneous lidar and radar measurements at McMurdo/Scott Base (77.8°S, 166.7°E), *J. Geophys. Res. Atmos.*, *118*, 2794–2808, doi:10.1002/jgrd.50318.

Chen, C., X. Chu, J. Zhao, B. R. Roberts, Z. Yu, W. Fong, X. Lu, and J. A. Smith (2016), Lidar observations of persistent inertia-gravity waves with periods of 3–10 h in the Antarctic middle and upper atmosphere at McMurdo, *J. Geophys. Res. Space Physics*, *121*, 1483–1502, doi:10.1002/2015JA022127.

Chu, X., C. Yamashita, P. J. Espy, G. J. Nott, E. J. Jensen, H.-L. Liu, W. Huang, and J. P. Thayer (2009), Responses of polar mesospheric cloud brightness to stratospheric gravity waves at the South Pole and Rothera, Antarctica, *J. Atmos. Sol. Terr. Phys.*, *71*, 434–445, doi:10.1016/j.jastp.2008.10.002.

Dowdy, A. J., R. A. Vincent, M. Tsutsumi, K. Igarashi, Y. Murayama, W. Singer, and D. J. Murphy (2007), Polar mesosphere and lower thermosphere dynamics: 1. Mean wind and gravity wave climatologies, *J. Geophys. Res.*, *112*, D17104, doi:10.1029/2006JD008126.

Duck, T. J., J. A. Whiteway, and A. I. Carswell (2001), The gravity wave-Arctic stratospheric vortex interaction, *J. Atmos. Sci.*, *58*, 3581–3596, doi:10.1175/1520-0469(2001)058<3581:TGWASV>2.0.CO;2.

Ehard, B., B. Kaifler, N. Kaifler, and M. Rapp (2015), Evaluation of methods for gravity wave extraction from middle-atmospheric lidar temperature measurements, *Atmos. Meas. Tech.*, *8*, 4645–4655, doi:10.5194/amt-8-4645-2015.

Fleming, E. L., S. Chandra, J. J. Barnett, and M. Corney (1990), COSPAR international reference atmosphere, chap. 2. Zonal mean temperature, pressure, zonal wind, and geopotential height as a function of latitude, *Adv. Space Res.*, *10*(12), 11–59.

France, J. A., V. L. Harvey, C. E. Randall, M. H. Hitchman, and M. J. Schwartz (2012), A climatology of stratopause temperature and height in the polar vortex and anticyclones, *J. Geophys. Res.*, *117*, D06116, doi:10.1029/2011JD016893.

Fritts, D. C., and M. J. Alexander (2003), Gravity wave dynamics and effects in the middle atmosphere, *Rev. Geophys.*, *41*(1), 1003, doi:10.1029/2001RG000106.

Geller, M. A., et al. (2013), A comparison between gravity wave momentum fluxes in observations and climate models, *J. Clim.*, *26*, 6383–6405, doi:10.1175/JCLI-D-12-00545.1.

Hauchecorne, A., and M. L. Chanin (1980), Density and temperature profiles obtained by lidar between 35 and 70 km, *Geophys. Res. Lett.*, *7*(8), 565–568, doi:10.1029/GL007i008p00565.

Hitchman, M. H., J. C. Gille, C. D. Rodgers, and G. Brasseur (1989), The separated polar winter stratopause: A gravity wave driven climatological feature, *J. Atmos. Sci.*, *46*, 410–422.

Holton, J. R. (1983), The influence of gravity wave breaking on the general circulation of the middle atmosphere, *J. Atmos. Sci.*, *40*(10), 2497–2507, doi:10.1175/1520-0469(1983)040<2497:TIOGWB>2.0.CO;2.

Kaifler, B., F. J. Lübken, J. Höffner, R. J. Morris, and T. P. Viehl (2015), Lidar observations of gravity wave activity in the middle atmosphere over Davis (69°S, 78°E), Antarctica, *J. Geophys. Res. Atmos.*, *120*, 4506–4521, doi:10.1002/2014JD022879.

Leovy, C. (1964), Simple models of thermally driven mesospheric circulation, *J. Atmos. Sci.*, *21*(4), 327–341.

Lindzen, R. S. (1981), Turbulence and stress owing to gravity wave and tidal breakdown, *J. Geophys. Res.*, *86*(C10), 9707–9714, doi:10.1029/JC086iC10p09707.

Liu, X., J. Yue, J. Xu, L. Wang, W. Yuan, J. M. Russell III, and M. E. Hervig (2014), Gravity wave variations in the polar stratosphere and mesosphere from SOFIE/AIM temperature observations, *J. Geophys. Res. Atmos.*, *119*, 7368–7381, doi:10.1002/2013JD021439.

Lu, X., X. Chu, W. Fong, C. Chen, Z. Yu, B. R. Roberts, and A. J. McDonald (2015), Vertical evolution of potential energy density and vertical wave number spectrum of Antarctic gravity waves from 35 to 105 km at McMurdo (77.8°S, 166.7°E), *J. Geophys. Res. Atmos.*, *120*, 2719–2737, doi:10.1002/2014JD022751.

Matsuno, T. (1982), A quasi one-dimensional model of the middle atmosphere circulation interacting with internal gravity waves, *J. Meteorol. Soc. Jpn. Ser. II*, *60.1*, 215–226

Mihalikova, M., K. Sato, M. Tsutsumi, and T. Sato (2016), Properties of inertia-gravity waves in the lowermost stratosphere as observed by the PANSY radar over Syowa Station in the Antarctic, *Ann. Geophys.*, *34*, 543–555, doi:10.5194/angeo-34-543-2016.

Rienecker, M. M., et al. (2011), MERRA: NASA's Modern-Era Retrospective Analysis for Research and Applications, *J. Clim.*, *24*, 3624–3648.

Shibuya, R., K. Sato, Y. Tomikawa, M. Tsutsumi, and T. Sato (2015), A study of multiple tropopause structures caused by inertia gravity waves in the Antarctic, *J. Atmos. Sci.*, *72*, 2109–2130, doi:10.11175/JAS-D-14-0228.1.

Stevens, M. H., L. E. Deaver, M. E. Hervig, J. M. Russell III, D. E. Siskind, P. E. Sheese, E. J. Llewellyn, R. L. Gattinger, J. Höffner, and B. T. Marshall (2012), Validation of upper mesospheric and lower thermospheric temperatures measured by the Solar Occultation for Ice Experiment, *J. Geophys. Res.*, *117*, D16304, doi:10.1029/2012JD017689.

Suzuki, H., Nakamura, T., Ejiri, M. K., Abo, M., Kawahara, T.D., Tomikawa, Y., and Tsutsumi, M. (2012), A Rayleigh Raman lidar system for troposphere-mesosphere observations at Syowa station, Antarctica, Reviewed and Revised Papers Presented at the 26th International Laser Radar Conference (ILRC 2012), S9P-18.

Whiteway, J. A., and A. I. Carswell (1994), Rayleigh lidar observations of thermal structure and gravity wave activity in the high Arctic during a stratospheric warming, *J. Atmos. Sci.*, *51*.21, 3122–3136, doi:10.1175/1520-0469(1994)051<3122:RLOOTS>2.0.CO;2.

Wright, C. J., N. P. Hindley, A. C. Moss, and N. J. Mitchell (2015), Multi-instrument gravity-wave measurements over Tierra del Fuego and the Drake Passage—Part 1: Potential energies and vertical wavelengths from AIRS, COSMIC, HIRDLS, MLS-Aura, SAAMER, SABER and radiosondes, *Atmos. Meas. Tech.*, *8*(7), 6797–6876, doi:10.5194/amtd-8-6797-2015.

Yamashita, C., X. Chu, H. L. Liu, P. J. Espy, G. J. Nott, and W. Huang (2009), Stratospheric gravity wave characteristics and seasonal variations observed by lidar at the South Pole and Rothera, Antarctica, *J. Geophys. Res.*, *114*, D12101, doi:10.1029/2008JD011472.

Yoshiki, M., and K. Sato (2000), A statistical study of gravity waves in the polar regions based on operational radiosonde data, *J. Geophys. Res.*, *105*(D14), 17,995–18,011, doi:10.1029/2000JD900204.

Yoshiki, M., N. Kizu, and K. Sato (2004), Energy enhancements of gravity waves in the Antarctic lower stratosphere associated with variations in the polar vortex and tropospheric disturbances, *J. Geophys. Res.*, *109*, D23104, doi:10.1029/2004JD004870.

Zhao, J., X. Chu, C. Chen, X. Lu, W. Fong, Z. Yu, R. Michael Jones, B. R. Roberts, and A. Dörnbrack (2017), Lidar observations of stratospheric gravity waves from 2011 to 2015 at McMurdo (77.84°S, 166.69°E), Antarctica: 1. Vertical wavelengths, periods, and frequency and vertical wave number spectra, *J. Geophys. Res. Atmos.*, *122*, 5041–5062, doi:10.1002/2016JD026368.